The use of different metal catalysts for the simultaneous production of carbon nanotubes and hydrogen from pyrolysis of plastic feedstocks

Jonathan C. Acomb[a], Chunfei Wu[b] and Paul T. Williams[a*]

[a] Energy Research Institute, University of Leeds, Leeds LS2 9JT, UK
Tel: #44 1133432504; Email: p.t.williams@leeds.ac.uk)
[b] Chemical Engineering, School of Engineering, University of Hull, Hull, HU6 7RX, UK

Abstract

Nickel, iron, cobalt and copper catalysts were prepared by impregnation and used to produce carbon nanotubes and hydrogen gas from a LDPE feedstock. A two stage catalytic pyrolysis process was used to enable large yields of both products. Plastics samples were pyrolysed in nitrogen at 600°C, before the evolved gases were passed to a second stage and allowed to deposit carbon onto the catalyst at a temperature of 800°C. Carbon nanotubes were successfully generated on nickel, iron and cobalt but were barely observed on the copper catalyst. Iron and nickel catalysts gave the largest yield of both hydrogen and carbon nanotubes as a result of metal-support interactions which were neither too strong, like cobalts, nor too weak like copper. These metal support interactions proved a key factor in CNT production.A nickel catalyst with a weaker interaction was prepared using a lower calcination temperature. Yields of both carbon nanotubes and hydrogen gas were lower on the Ni-catalyst prepared at the lower calcination temperature, as a result of sintering of the nickel particles. In addition, thecatalyst prepared at a lower calcination temperature produced metal particles which were too large for CNT growth, producing amorphous carbons which deactivate the catalyst instead. Overall the iron catalyst gave the largest yield of CNTs, which is attributed to both its good metal-support interactions and irons large carbon solubility.

1 Introduction

Thermal treatments such as pyrolysis are well-known methods for producing valuable gases and liquids from hydrocarbon feedstocks [1-3]. Among the gases produced, hydrogen is of particular interest as it is considered an important future fuel, since its combustion gives off only water. Whilst hydrogen is predominantly produced from reforming of natural gas, thermal treatment of hydrocarbon feedstocks such as waste plastics offer a more environmentally sound solution. Waste plastics are notoriously difficult to recycle, and thermal treatments such as pyrolysis can therefore offer an alternative waste management option to unsustainable landfill practices. Production of hydrogen from waste plastics is therefore a well-researched area, with a number of studies using pyrolysis and gasification techniques [4-9].

Transition metal e.g. nickel based catalysts are typically used for hydrogen production as they offer a higher catalytic activity than other transition metals, but are cheaper than other effective metal catalysts such as the noble metals [10]. However a major problem associated with using transition metal based catalysts in thermal treatment of hydrocarbons is deactivation by coking [11], where carbon deposition builds on the catalyst surface. In an investigation into carbon deposition onto nickel catalysts Rostrup-Nielsen found three distinct types [12]. These were whisker type carbons, such as filamentous carbons, and pyrolytic and encapsulating carbons which deactivate the catalyst. As such a number of studies have aimed to reduce the build-up of carbon deposition on catalysts, in order to keep catalyst activities high [13-16].

However, recently it has been shown that some of the carbon deposits produced during plastics pyrolysis are valuable carbon nanotubes, with Kukovitsky et al. demonstrating production of crooked carbon nanotubes and filamentous carbons from pyrolysis of LDPE at

450°C [17]. Carbon nanotubes are a valuable form of carbon with an increasingly large number of publications on the subject due to their potential for current and future uses in a wide range of industries including composites, microelectrics and energy applications [18, 19]. Current mass production of CNTs comes from chemical vapour deposition of hydrocarbon gases such as methane and acetylene, however the pull of a low cost alternative which tackles waste management problems has encouraged research into production from plastic sources. As a result, a number of studies have started to tailor their pyrolysis processes towards carbon nanotube production, achieving large yields with temperatures up to 900°C [17, 20-27]. Using a two stage process also enables large yields of hydrogen gas and carbon nanotubes can be produced simultaneously from a plastic source [20, 26, 28]. In previous studies by this research group a two stage process was devised where evolved pyrolysis gases were passed directly into the second catalysis stage [20, 28]. A nickel catalyst was used, and large amounts of carbon nanotubes were produced in addition to large yields of hydrogen.

Catalysts play a key role in the production of carbon nanotubes and hydrogen. Whilst nickel catalysts excel at hydrogen production and are known to produce CNTs, other transition metals have also been researched for their potential for CNT production via CVD. Along with nickel, the most commonly used catalyst metals are iron [29-35], cobalt [36-38] and copper [39]. When catalyst metals have been directly compared it has been found that whilst all the metals are able to produce CNTs, iron catalysts give a large yield [31, 33, 35, 40]. Liu et al [40] investigated the effect of using iron, cobalt and nickel catalysts on CNT production from CVD of methane. The superior performance of the iron catalyst was attributed to irons higher carbon solubility, which helps to promote the production of carbon nanotubes. In terms of hydrogen production however, iron and copper catalysts have shown much lower hydrogen yields than nickel and cobalt during steam reforming [10, 41]. However, hydrogen

is also produced during carbon deposition. When investigating the decomposition of methane into carbon nanotubes and hydrogen, Ago et al. found that decomposition was higher in iron catalysts than cobalt and nickel [29], producing higher hydrogen yields as a result.

In addition to the influence of metal types on CNT and hydrogen productions, the calcination temperature used during catalyst preparation is also an important factor [36, 42-44]. For example, Chai et al. investigated the effect of the calcination temperature of a cobalt catalyst on CNT production using methane in a CVD process [36]. At low calcination temperatures, the interaction between the catalyst metal and support was weak, and during CNT production the catalyst underwent sintering, leading to metal particles too large for CNT production. As the calcination temperature was increased, however, the metal support interaction became stronger and as a result, the carbon nanotube yield increased. This was only true up to a certain point however, as the catalyst can become hindered by too strong a metal support interaction [45]. The calcination temperature likewise has an effect on hydrogen production [46-48]. Garcia et al [48] investigated the effect of calcination temperature on hydrogen production and found that whilst lower calcination temperatures gave higher yields in the short term, the increased stability achieved with a higher calcination temperature led to a better overall performance in terms of long-term hydrogen production.

Currently, to our best knowledge, little information could be found on the investigation of different metal active sites and calcination temperatures on the simultaneous production of CNTs and hydrogen from pyrolysis of plastics. In this paper, a two stage catalytic pyrolysis process will be used to produce carbon nanotubes and hydrogen simultaneously. The effect of catalysts prepared using different metals and calcination temperatures will be investigated to determine the optimum catalyst for the process. Nickel, iron, cobalt and copper catalysts will all be considered.

2 Experimental

2.1 Materials and reaction system

A low density polyethylene (LDPE) sample was obtained from ACROS Organics UK.

Nickel, iron, cobalt and copper catalysts were prepared by an impregnating the metal onto an alumina support, so that a 10 wt% metal catalyst was produced. Metal nitrates and gamma Al_2O_3 were used as the raw materials. The metal nitrate was dissolved in ethanol, following which the alumina was added and the mixture left until it formed a slurry. This was then dried overnight in an oven at 50°C to remove the remaining ethanol before calcination was undertaken. Two different calcination temperatures of 500 and 750°C were used for the nickel catalyst to investigate the effect on CNT and H_2 production. The catalysts were heated to the desired temperature at a heating rate of 2°C/min in an air atmosphere with a hold time of 3h. Iron, cobalt and copper catalysts were also prepared using the same methodology, using a 750°C calcination temperature. The catalysts were then crushed and sieved to give granules of between 0.05 and 0.18 mm.

The experimental system consisted of a two-stage pyrolysis reactor as shown in Fig. 1. The reactor was made of stainless steel and had a total length of 320 mm and an internal diameter of 22 mm The top and bottom reactors were heated by separate furnaces. In each experiment 1 g of the LDPE was placed inside a sample boat and pyrolysed in first reactor, where the temperature was heated to 600°C. The generated gaseous products were then passed through to the second reactor, held at 800°C, and passed over 0.5 g of catalyst, allowing hydrogen to be produced with carbon deposition on the catalyst. Nitrogen was used as the carrier gas with

a flow rate of 80 ml min^{-1}. The procedure was to heat the second gasification reactor to the desired temperature, then heat the first reactor to 600°C at a heating rate of 50°C min^{-1} for a total reaction time of 30 min. The volatile products after the gasification process were passed through two condensers, where any condensed products were collected. The non-condensed gases were collected in a 25 l Tedlar™ gas sample bag. The reproducibility of the reaction system was tested and experiments were repeated to ensure the reliability of research results.

The gases collected in the gas sample bag were analysed by packed column gas chromatography (GC). Hydrocarbons (C_1–C_4) were analysed using a Varian 3380 gas chromatograph with a flame ionisation detector, with an 80–100 mesh Hysep column and nitrogen carrier gas. Permanent gases (H_2, CO, O_2 and N_2) were analysed with a separate Varian 3380 GC/TCD, thermal conductivity detector, with two packed columns. A 2 m long and 2 mm diameter column packed with 60–80 mesh molecular sieve was used to analyse hydrogen, nitrogen, carbon monoxide and oxygen. Carbon dioxide was analysed on a 2 m long and 2 mm diameter column with Haysep 60–80 mesh molecular sieve. The carrier gas was argon.

2.2 Characterisation of catalyst

The fresh catalysts were investigated by a series of analyses. High resolution transmission electron microscopy was undertaken, with EDX carried out in conjunction. TEM was undertaken on an FEI Tecnai TF20 with EDX provided by an Oxford Instruments INCA 350 EDX system. X ray diffraction (XRD) of the fresh catalysts was undertaken with a Bruker D-8 diffractometer using a Cu-Ka X-ray source with a Vantec position sensitive detector. Temperature programmed reduction of the nickel catalysts was undertaken using a Stanton-Redcroft thermogravimetric analyser. The samples were heated at 20°C min^{-1} up to 150°C to

remove moisture, and then held for 30 min in a hydrogen atmosphere (5% H_2 balanced with N_2). The samples were then heated in the hydrogen atmosphere at 10 $Cmin^{-1}$ to 900°C.

Carbon deposition on the used catalysts was analysed by a range of techniques in order to characterise the nature of the carbon that was deposited on the surface of the catalysts during the experimental procedure. Electron microscopy was undertaken on the used catalysts, with SEM and TEM both employed. A LEO 1530 and Hitachi SU8230 were used for SEM.

The reacted catalysts were analysed by temperature programmed oxidation to investigate the types and relative amounts of carbon deposits on their surfaces. Around 20 mg of the reacted catalyst was heated in a thermogravimetric analyser in an atmosphere of air at a heating rate of 15°C min^{-1} up to a temperature of 800°C and with a hold time of 10 min. XRD diffraction on the used catalyst samples was also undertaken.

Raman spectroscopy was undertaken on the carbon deposits on the catalyst surface to determine their graphitic quality. Results were obtained using a Renishaw Invia Raman spectrometer at a wavelength of 514 nm at Raman shifts between 100 and 3200 cm^{-1}.

3 Results and discussion

3.1 Influence of catalyst metal

3.1.1 Characterisation of fresh catalysts

In order to better understand the properties of the catalysts used, a number of analyses were carried out on the fresh catalysts. TEM-EDX, XRD and TPR were all undertaken.

3.1.1.1 Nickel alumina

The TEM image of the Nickel catalyst in Figure 2(a) shows a particle which is very uniform in its structure. EDX spectrums (Supporting Information) were taken for the whole catalyst particle, as well as two points in different regions of the catalyst surface. The spectrum obtained for the area A1 showed the presence of Al, Ni and O, which is expected of the Ni/Al_2O_3 catalyst. The spectrums of points 1 and 2 both show peaks for Al, Ni and O suggesting that the particle is consistent throughout, with nickel, aluminium and oxygen all bonded together.

Results from XRD of the Nickel catalyst, seen in Figure 3, show peaks associated with $NiAl_2O_4$ and Al_2O_3 and small peaks for NiO. Nickel aluminate is formed at high calcination temperatures such as the one used in this study [49, 50], when NiO bonds to the alumina support. The XRD results conform with the TEM-EDX images in showing the presence of catalyst is largely comprised of nickel, aluminium and oxygen bonded together as a nickel aluminate.

TPR results for the nickel catalyst are shown in Figure 4, with a large peak observed at 800°C. A number of studies have found similar results and attribute the peak to the reduction of nickel aluminate [48, 51, 52]. Again this agrees well with previous analyses in identifying the catalyst as predominantly composed of nickel aluminate. NiO particles were not clearly identified from the TEM or TPR analyses, implying that only very small quantities were present.

3.1.1.2 Iron alumina

The TEM image in Figure 2(b) for the iron catalyst shows differences to the nickel catalyst with two different phases in the catalyst observed. The EDX spectrum (Supporting

Information) for the area A1 showed peaks for Fe, Al and O, consistent with an iron alumina catalyst. However, there are notable differences in the spectrums of point A and point B representing the different parts of the catalyst. Whilst point B showed Fe, Al and O, point one only produced peaks for Fe and O. This suggests that a form of iron oxide is produced. The particles of iron oxide observed had diameters ranging from 20 – 100 nm. The presence of iron oxide suggests that not all the iron is bonded to the alumina as an aluminate as was the case with the nickel catalyst prepared at the same conditions. This is in accordance with literature which reports that iron forms aluminates less readily than nickel [53].

XRD results, shown in Figure 3, support the conclusions drawn from the TEM-EDX analysis, with both Fe_2O_3 and Al_2O_3 present in the catalyst. TPR results in Figure 4 show that the iron catalyst produces a broad peak at 450°C, with a further series of peaks at temperatures between 700 and 850°C. The reduction of iron oxide supported on alumina is complex and occurs in a number of stages [54-56]. Park et al report that a first peak between 400 and 560 °C is related to the conversion of Fe_2O_3 into Fe_3O_4, which subsequently is reduced into FeO and Fe metal at 600-800°C [56]. As such, the first peak observed in TPR represents the first stage of reduction into Fe_3O_4, whilst further peaks represent the subsequent reduction to and Fe. Iron aluminate is reported to reduce at temperatures above 850°C [57], and so the peak observed above 800°C could be related to this. It is suggested that the iron catalyst contains iron oxide which has not bonded to the alumina to form an aluminate. The main TPR peak for the iron catalyst is at a lower temperature than that of the nickel catalyst, indicating the iron is more easily reduced, and so less strongly bonded to its alumina support.

3.1.1.3 Cobalt alumina

Similarly to nickel, the cobalt catalyst also shows a uniform structure in its TEM image in Figure 2(c). The EDX spectrum (Supporting Information) obtained for the whole particle in area A1, showed the presence of Co, O, and Al, consistent with a Co/Al_2O_3 catalyst. To gain more insight into the catalyst structure, as with the other catalysts, two EDX spectrums of specific points on the catalyst surface were obtained (Supporting Information). Both the points revealed the presence of Co, O and Al, suggesting that as with nickel, the catalyst is all in one phase with Co bonded to the alumina.

XRD results in Figure 3 show the presence of $CoAl_2O_4$ along with alumina, consistent with TEM-EDX results in portraying a catalyst with cobalt bonded to the alumina support. The lack of cobalt oxide agrees well with literature since Co is reported to form aluminates more readily than both nickel and iron [53]. TPR results (Figure 4) for cobalt show no significant peak associated with reduction in the temperature range tested. Previous TPR studies however do not report reduction of cobalt aluminate until temperatures of 1200K; higher than the cobalt catalyst used in our analysis [58]. Along with the lack of a significant peak at lower reduction temperatures, this leads to the suggestion that the cobalt in the catalyst is present in the form of cobalt aluminate. This is in agreement with both TEM-EDX and XRD analyses, and suggests the cobalt is very strongly bonded to the alumina, since it is hardly reduced at temperatures below 900°C.

3.1.1.4 Copper alumina

Like the cobalt and nickel catalysts, the TEM image of the fresh copper catalyst in Figure 2(d) is fairly uniform. The EDX spectrum (Supporting Information) of the whole catalyst particle predictably is comprised of peaks for Cu, Al and O, whilst the spectrums from points

1 and 2 also show the same result. As with the nickel and cobalt catalysts this shows that the copper catalyst is consistent throughout, suggesting a single phase composition such as copper aluminate.

XRD results, shown in Figure 3, confirm the presence of $CuAl_2O_4$, with alumina present. TPR results from the copper catalyst, Figure 4, show a large peak at around 200°C in addition to a broad peak between 350 and 650C. These results are consistent with the reduction of CuO and $CuAl_2O_4$ for the low and high temperature peaks, respectively [59, 60]. CuO was barely observed in XRD, however Luo et al found similar results [59], and attributed the lack of CuO in XRD to its highly disperse nature. As such it is thought that the peak observed in this case is similarly highly disperse CuO which has not formed into bulk CuO.

3.1.2 Mass balance and hydrogen production

Results for the mass balance in terms the amount of gases, solids and liquids produced from all the experiments can be seen in Table 1, where solids constitute carbon deposition on the catalyst, and the small amounts of wax also obtained. In terms of the performance of different metals, iron produced a smaller amount of gases than nickel, with a much larger yield of solids. Cobalt and copper on the other hand produce results far more comparable to the nickel catalyst in terms of gases, solids and liquids with both producing only slightly more oils and less solids than nickel.

Gas compositions and hydrogen conversions for the different catalysts are seen in Table 1. The hydrogen conversion is based upon the amount of hydrogen in the LDPE sample from results obtained from an elemental analysis. Whilst the amount of gases produced from iron was less compared to nickel, the relative concentration of hydrogen in the gas is significantly

higher and the concentrations of hydrocarbons are lower. This results in a large hydrogen conversion of 26.8%. Cobalt and copper catalysts however produce a lower yield of hydrogen than the other catalysts, with conversion values of 12.8% and 10.1% for cobalt and copper respectively, compared with a value of 16.1% for nickel. Nickel catalysts are widely reported to be effective at hydrogen production when compared to iron, cobalt and copper, however in this instance it has been outperformed by iron. The large yield for iron in this instance could be due to the fact that a larger amount of carbon deposition occurred, as shown by its high solid yield in the mass balance. Since hydrogen is given off during carbon deposition, a larger amount of carbon would result in a corresponding high yield in hydrogen. It is noted that steam was not introduced in the experiment; therefore catalytic thermo-cracking reactions are dominant during the pyrolysis of plastics.

3.1.3 Carbon nanotube production

3.1.3.1 Scanning and Transmission Electron Microscopy

Both scanning electron microscopy (SEM) and transmission electron microscopy (TEM) were undertaken on the used catalysts in order to investigate the carbon deposition on the surface, with particular interest in carbon nanotubes. SEM images of the nickel catalyst are shown in Figure 5(a), where the catalyst shows a covering of filamentous carbons. TEM images shown in Figure 6(a) confirmed that the filaments observed were carbon nanotubes. The carbon nanotubes had diameters between 15 – 30 nm and lengths of up to a number of μm. The images reveal the presence of carbon nanotubes, and bamboo type carbon nanotubes, along with a number of loose metal particles, which have separated from the

catalyst surface. Metal particles are also seen inside the carbon nanotubes, indicating the tip, rather than base growth mechanism.

Like the SEM images for nickel catalyst, the images seen for iron in Figure 5(b) also show a dense covering of the catalyst surface in filamentous carbons. TEM images in Figure 6 (b) confirm the presence of carbon nanotubes, which are multiwalled, with bamboo type carbon nanotubes also observed. Similarly to those produced using the nickel catalyst, the carbon nanotubes had diameters between 15 – 30 nm and lengths of up to a number of μm. The TEM images also show the presence of a greater number of metal particles than was observed on the nickel catalyst, and CNTs with a larger diameter. Larger diameter CNTs are thought to be produced from larger metal particles [45, 61, 62], which could have formed as a result of the weaker metal support interaction the iron catalyst demonstrates. A weaker support interaction would allow sintering of the iron to form larger metal particles. The weak support interaction would also explain the presence of a larger amount of loose metal particles, since they would separate from the support more readily.

The SEM images from the cobalt catalyst are seen in Figures 5(c). The images show the presence of long thin filamentous carbons. However they are not as densely packed as on the surface of the iron or nickel catalysts, suggesting that less are produced. TEM images in Figures 6(c) also confirmed the presence of multiwalled carbon nanotubes. The CNTs show a much narrower diameter, and very few loose metal particles. The carbon nanotubes had diameters between 5 – 20 nm and lengths of up to a number of μm. TPR results (Fig.4) revealed cobalt to have a very strong support interaction, which would restrict sintering of the metal catalyst and result in smaller CNT diameters as a result. It is also possible that the strong interaction could inhibit the production of CNTs, by restricting sintering to such an extent that the metal particles formed are either too small for CNT growth or too strongly

attached. The strong metal-support interaction would also prevent metal particles from becoming detached from the catalyst surface, supporting the lack of metal particles observed from this catalyst.

The copper catalyst in contrast to the other metals shows almost no filamentous carbons on the SEM image in Figure 5(d). This indicates that almost no carbon nanotubes were produced on this catalyst. TEM images of the catalyst in Figure 6(d) accordingly only showed the presence of amorphous carbons, with no filamentous or carbon nanotubes observed. The TEM image revealed very large metal particles produced on the copper catalyst, indicating the presence of copper oxides particles revealed by the TPR (Figure 4). It is suggested that the dispersed CuO particles can be easily reduced (Figure 4), leading to a significant amount of sintering and metal particles which are too large to form carbon nanotubes.

3.1.3.2 X-Ray Diffraction of the used catalysts

XRD of the used catalysts are shown in Figure 7. The nickel, iron, cobalt and copper in the catalysts were all reduced to their metallic form, with no other oxides or aluminates of the metals observed. This indicates that the metal oxides and aluminates were all reduced by reducing agents e.g. hydrogen in the pyrolysis gases in situ. The nickel and iron catalysts also show a peak for graphitc carbon, indicating significant carbon formation on the surfaces of these catalysts.

3.1.3.3 Temperature programmed oxidation

Temperature programmed oxidation of the catalysts was undertaken to give a better understanding of the types of carbon deposited on the catalyst surface and their abundance. TPO of the catalysts gave two peaks around 550°C and around 650°C on the derivative plot, seen in Figure 8(a). Amorphous carbons are reported to show a peak at lower temperatures

than filamentous carbons, due to being more reactive [63]. As such the low temperature peak is associated with the oxidation of amorphous carbons whilst the high temperature peak is associated with the oxidation of filamentous carbons. Since all the filamentous carbons observed from TEM were CNTs, it is a fair assumption that the peak associated with filamentous represents CNTs alone. The nickel catalyst shows the peaks associated with amorphous and filamentous carbons on the derivative TPO plot, shown in Figure 8(a). Both peaks are of a similar size, suggesting both carbon types are produced in roughly equal amounts. Based on the TPO results, calculations were undertaken to determine the amount of each carbon type, with results shown in Figure 8(b). The nickel catalyst produced a yield of 49.9 mg/g plastic of amorphous carbons and 45.7 mg/g plastic of CNTs. This is lower than was obtained in a previous study by this research group using a similar conditions, but with a different catalyst preparation technique [20]. The lower yield is likely due to a change in reactor design altering the pyrolysis gases obtained.

TPO plots for the iron catalyst in Figure 8(a) likewise show the presence of two peaks, associated with amorphous carbons and CNTs, however, unlike the nickel catalyst the filamentous peak is much larger. The values associated with each type of carbon were found to be 8 and 179 mg/g plastic for amorphous and CNTs, respectively. This shows that the iron catalyst produced a great deal more carbon nanotuobes than its nickel counterpart. This is consistent with a number of studies which have reported iron to give higher yields of CNTs than other transition metals [31, 33, 35, 40]. This also agrees well with the larger hydrogen yield from the iron catalyst, since a larger amount would be produced during the deposition of CNTs.

Whilst carbon nanotubes were observed on the cobalt catalyst, TPO plots seen in Figure 8(a) suggest that the predominant type of carbon deposition was amorphous carbons. This is

because the oxidation peak associated with filamentous carbons is much smaller than that of the amorphous carbons. The values for each types of carbon calculated mirror this, with amorphous carbons, 68 mg/g plastic, vastly outweighing filamentous carbons, 6 mg/g plastic. This is in accordance with the SEM images since less filamentous carbons were obtained than for both the nickel and iron catalysts. It also indicates why no significant peak for carbon was observed in XRD (Fig. 7). The results show that the cobalt catalyst clearly favours the production of amorphous carbons over filamentous carbons and is not an effective catalyst for carbon nanotube production. This is consistent with other studies comparing cobalt with iron catalysts, where cobalt proved less effective for CNT production [31, 33, 35, 40]. Similarly low yields of CNTs were also obtained from a cobalt catalyst containing $CoAl_2O_4$ by Chai et al [36], where metal-support interactions were too strong and inhibited CNT growth.

TPO results for copper, shown in Figure 8(a), reinforce the findings from electron microscopy with no peak seen for filamentous carbons. Peaks for amorphous carbons are observed, and gave a value for amorphous carbon deposition of 47 mg/g plastic. The small amount of carbon deposition on the used copper catalyst ties in with XRD, where no significant peak was observed. This demonstrates that copper is not a suitable catalyst for the production of carbon nanotubes from a plastic feedstock.

3.1.3.4 Raman Spectroscopy

Raman spectroscopy is an analytical technique that can be used to characterise CNTs. Spectrums produced (Figure 9) show peaks at 1589 and 1348 cm^{-1} corresponding to the G peak, associated with graphitic carbon structures within the sample, and the D peak associated with defects within the graphic lattice or amorphous carbons, respectively [64]. A

G’ peak is also observed at 2709 cm^{-1} associated with the two photon elastic scattering process, and can be used as an indicator of the purity of carbon nanotubes. The ratio between the height of these peaks, G:D ratio, is often used as a tool to determine the quality of CNTs produced with a higher value representing better quality or purity CNTs [65]. Figure 9(a) shows that the spectrum obtained for the nickel catalyst, shows the presence of the G and D peaks that are commonly associated with carbon nanotubes and gave a G:D ratio of 1.35. Raman spectroscopy of the used iron catalyst (Figure 9(b)) likewise showed G and D peaks. In comparison to the nickel catalyst however, the size of the D peak is much smaller. The G:D ratio of the iron catalyst is accordingly higher than that obtained for nickel, with a values of 1.96, indicating of a higher purity of carbon nanotubes. A strong G’ peak is observed for the carbon deposits from both the nickel and iron catalysts, indicating good CNT purity.

The cobalt catalyst gave a Raman spectrum, shown in Figure 9(c), with G and D peaks of a similar size. The corresponding G:D ratio obtained was 1.22; smaller than obtained for the iron and nickel catalysts. This correlates with the other analyses in suggesting that the purity and quantity of carbon nanotubes is lower for the cobalt catalyst. Raman spectroscopy of the copper catalyst (Figure 9(d)) shows two small peaks at the G and D position. The G:D ratio obtained is low at a value of 1.18, also indicating the poor quality of carbon deposits obtained from this catalyst. The copper catalyst showed that carbon deposits have almost no carbon nanotubes from TEM which would account for the low ratio obtained. In addition, the Raman spectrum for the carbon deposits on the copper catalyst showed no G’ peak. This is in contrast to those on iron, nickel and cobalt which saw this peak, again suggesting no carbon nanotubes on the copper catalyst.

3.1.4 Discussion

The results show that the catalyst metal used has a strong influence on the CNT yield, with catalyst support interactions playing an important role. TPR and TEM analyses showed that the cobalt had a strong interaction with the alumina, which prevented the formation of metal particles that could readily detach from the catalyst surface or were of a suitable size for CNT growth. Whilst the cobalt catalyst had a metal-support interaction which was too strong, the disperse copper oxide particles in the copper-based catalyst could be easily reduced (TPR results, Figure 4); as a result, a great deal of sintering of copper occurred, leading to the large particles observed in TEM for the reacted catalyst which proved that copper based catalyst is unsuitable for CNT production in this work. The nickel and iron catalysts in contrast showed metal-support interactions which were suitable for CNT production, since both gave significant yields. The TPR results showed that these catalysts gave reduction peaks at intermediate values between 400 and 900°C, which were clearly associated with support interactions which were neither too weak nor too strong.

TEM images also showed that these catalysts had a great deal more loose metal particles than the cobalt catalyst, suggesting the ability of metals to detach from the surface could be an important factor in CNT growth. As reviewed by Tessonnier et al. [66], metal particles play an important role during the vapour-solid-solid growth mechanism, affecting the decomposition of carbon-containing precursors and diffusion of carbon atoms and also precipitation of carbon at the metal-support interface. It is suggested that CNT production is best suited to metal support interactions of intermediate strength. Chai et al. found similar results when investigating cobalt catalysts prepared at different calcination temperatures, with weaker interactions producing catalyst particles too large for CNT growth, but interactions which were too strong resulting in drastic reductions in CNT yield [36].

3.2 Effect of calcination temperature

In order to investigate the effect of metal support interactions further, a nickel catalyst was prepared at a lower calcination temperature of 500°C (Nickel500 as opposed to the Nickel750 catalyst). The effect of the resulting lower catalyst support interaction on the production of hydrogen and carbon nanotubes could then be determined.

3.2.1 Characterisation of fresh catalysts

The TEM image of the Nickel500 catalyst in Figure 10(a) reveals that it is made of two distinct phases. The EDX spectrum (Supporting Information) of the whole catalyst particle, in area A1, showed the presence of Ni, Al and O, consistent with the Ni/Al_2O_3 catalyst. EDX spectrums were also taken at the two different phases observed. The spectrum (Supporting Information) observed at point A showed peaks for Ni and O, indicating that this is a form of nickel oxide. In contrast the spectrum of point B showed Ni, Al and O suggesting the presence of nickel aluminate as was observed in the nickel catalyst prepared at 750°C. Nickel oxide is reported to interact with alumina at relatively low temperatures such as the 500°C calcination temperature used to form nickel aluminate, suggesting this could be compound formed [50].

XRD analysis of the Nickel500 catalyst has been carried out, with the results shown in Figure 10(b). It shows the presence of a number nickel and alumina compounds. The nickel in the catalyst is present as both NiO and $NiAl_2O_4$, with alumina present as Al_2O_3, reaffirming conclusions from SEM and TEM that the catalyst structure contains nickel oxide particles bonded to the alumina support in addition to nickel aluminate.

TPR of the catalyst calcined at 500°C shown in Figure 10(c) shows a large peak at around 725°C and a smaller peak at around 400°C. Peaks at 400 and 725°C are consistent with

literature with the reduction of NiO and $NiAl_2O_4$ respectively, on a nickel alumina catalyst prepared by impregnation [52]. The peak associated with the reduction of the nickel aluminate has shifted to a lower temperature compared to reduction obtained from the Nickel750 catalyst (Fig. 4). This agrees well with results obtained by Garcia et al., where a nickel catalyst calcined at a lower temperature gave a reduction peak at a lower temperature because of smaller amounts of nickel aluminate [48]. The presence of the NiO peak is consistent with TEM-EDX and XRD results (Fig. 10), which show that a lower calcination temperature leads to less of the nickel bonding to the catalyst support in the form of nickel aluminates, and instead remains as nickel oxide. This agrees well with work by Chen et al where nickel aluminate formation increases at higher calcination temperature through a reaction between the alumina support and NiO [49]. When compared to the catalyst prepared at a higher calcination temperature, the reduction peak has shifted to a lower temperature, indicating a weaker metal-support interaction. Overall the Nickel500 catalyst has a weaker metal-support interaction due to the presence of the nickel oxide, which is more easily reduced, and in turn appears to make the nickel aluminate more easily reducible.

3.2.2 Mass balance and hydrogen production

The product distribution in terms of gases solids and liquids for the Nickel500 catalyst is seen in Table 2 along with the composition of the gas stream. There is very little difference between the catalyst calcined at 500°C and 750°C, with both producing large amounts of gas and smaller amounts of solids and oils. The Nickel750 catalyst however does give a slightly larger hydrogen conversion of 16.5% compared with 15.2% for the 500°C catalyst. This result would suggest that the calcination temperature has not had a strong influence on hydrogen production in this instance.

3.2.3 Carbon nanotube production

3.2.3.1 Scanning and Transmission Electron Microscopy

The deposition on the Nickel500 catalyst in the SEM image in Figure 11(a) shows the presence of filamentous carbons on the catalyst surface. As was the case with the catalyst prepared at 750°C the TEM images shown in Figure 11(c) confirmed that the filaments observed were carbon nanotubes. The carbon nanotubes were similar to those produced on the Nickel750 catalyst and had diameters between 15 – 30 nm lengths of up to a number of μm. TEM images also show that similarly to the nickel and iron catalysts prepared at the higher calcination temperature, there are a number of loose metal particles. However, the size of these particles appears larger than was observed from the Nickel750 catalyst. This indicates that the weaker metal-support interaction, indicated by TPR, has allowed greater sintering of the nickel particles.

3.2.3.2 Temperature Programmed Oxidation

In TPO results in Figure 12(a) the peak associated with amorphous carbons is much larger than that of the filamentous carbons, showing that a larger amount of amorphous carbons have been produced. Calculations based upon these TPO results proved this to be the case with 65.0 and 17.7 mg/g plastic of amorphous and filamentous carbons produced respectively as shown in Figure 12(b). This is a smaller yield of CNTs than was obtained with the nickel catalyst prepared at a higher calcination temperature. As such the calcination temperature of the catalyst is an important factor in determining the yield of CNTs with a higher calcination temperature giving a larger amount of CNTs and smaller amounts of amorphous carbons. This strengthens the conclusion that the catalyst support interaction is an important factor in CNT growth, since a weaker interaction has yielded smaller amounts of CNTs. The larger

production of amorphous carbons on the Nickel500 compared to the Nickel750 catalyst could also be responsible for the smaller hydrogen yield, since amorphous carbons are known to deactivate catalysts by encapsulating catalyst particles [12].

3.2.3.3 Raman Spectroscopy

Raman analysis of the used Nickel500 catalyst is shown in Figure 11(b) show the presence of both G and D peaks, with the peaks being of a similar height. This gave a G:D ratio of 1.10, lower than was obtained for the Nickel750 catalyst indicating less purity in terms of CNTs. This is consistent with TPO results where the Nickel750 catalyst showed a larger yield of CNTs and smaller amounts of amorphous carbons.

3.2.4 Discussion

From the analyses on the fresh catalysts it was found that the lower calcination temperature produced weaker catalyst-support interactions, forming NiO rather than $NiAl_2O_4$. The interaction between the metal and support proved to be an important factor when using different catalysts, with the weak interaction of the copper catalyst allowing sintering of the metal to occur, and yielding catalyst particles which were too large for CNT production. Similarly, a larger yield of amorphous carbons, rather than CNTs, were produced from the catalyst with a lower calcination temperature as a result of its weaker metal support interaction.

The weaker metal-support interaction allowed sintering of the nickel, resulting in larger particles which yielded more amorphous carbons. Chai et al, found similar results where increasing the calcination temperature yielded more CNTs when using a cobalt catalyst and a methane feedstock [36]. It was suggested that at lower calcination temperatures, sintering produced catalyst particles too large to form CNTs. Liu et al also obtained higher yields of

CNTs with stronger catalyst support interactions when investigating different supports with an iron catalyst, again using methane as a feedstock [40].

Results show that the Nickel500 catalyst had a weaker metal support interaction than the Nickel750 catalyst, and produced less CNTs as a result. However TPR and TEM analyses showed that the iron catalyst had a similar interaction, but yielded significantly more CNTs. This suggests that catalyst support interactions are not the only factor governing CNT production. It has been suggested that iron catalysts in particular produce large yields of CNTs because of irons large carbon solubility compared to other metals [40]. Similarly, this could help to indicate why copper aluminate particles, which show a reduction peak comparable to iron and nickel, produce almost no CNTs, since copper has a much lower carbon solubility [67]. Carbon solubility is thought to be a key aspect of CNT growth, since it increases the amount of carbon available for CNT growth, and is thought to produce a higher concentration driving force which accelerates the CNT formation rate [40, 67]. In this instance, irons large CNT yield could be a result of a desirable catalyst-support interaction coupled with a large carbon solubility.

The CNTs produced from the thermal treatment of plastics on the iron, nickel and cobalt catalysts showed similar dimensions and characteristics to those produced from more standard means such as chemical vapour deposition [68-70]. As the carbon nanotubes in this study were produced from plastics, this provides a cheaper carbon source. This opens up the possibility of using the CNTs obtained in commercial applications, particularly if the iron catalyst was used, as this gave the highest yield. Studies have made use of multiwalled CNTs in a number of applications ranging from high strength composites, coatings, water treatment and energy technologies [19, 71-77]. In order to be used in these applications however, a purification process needs to be undertaken to remove amorphous carbons and other

contaminants from the CNTs. A purification stage would increase the cost of the CNTs produced, and so further study to make the process more economical will concentrate on switching to a continuous process, and increasing CNT yields through process optimization and the investigation of novel catalysts.

4 Conclusions

Carbon nanotubes and hydrogen gas were successfully produced simultaneously on nickel, iron and cobalt catalysts using a plastic feedstock. Bamboo type carbon nanotubes were also observed. Copper catalysts however produced almost no CNTs. It is suggested that the interaction between the catalyst metal and alumina support played a strong part in governing the yield of CNTs, with a too weak an interaction allowing sintering of metals to produce particles too large for CNT growth, and too strong an interaction hindering production. The nickel and iron catalysts proved to have an interaction which was neither too weak, like the copper catalyst, nor too strong, like the cobalt catalyst, resulting in significant CNT yields. CNT yields were as follows: Fe>Ni>Co>Cu, with the iron catalyst giving the largest yield with a value of 179 mg/g plastics. This work also shows that the iron-based catalyst giving the largest yield of hydrogen as opposed to the nickel catalyst which is traditionally used for hydrogen production.

Investigating the interaction between catalyst and support has been further carried out by developing Ni-based catalyst at different calcination temperatures. Results showed that the weaker interaction resulted in production of larger metal particles during the reaction, and hence a lower yield of carbon nanotubes was obtained.

References

1. Demirbas, A., *Pyrolysis of municipal plastic wastes for recovery of gasoline-range hydrocarbons.* Journal of Analytical and Applied Pyrolysis, 2004. **72**(1): p. 97-102.

2. He, M., et al., *Syngas production from catalytic gasification of waste polyethylene: Influence of temperature on gas yield and composition.* International Journal of Hydrogen Energy, 2009. **34**(3): p. 1342-1348.

3. Kodera, Y. and Y. Ishihara, *Novel Process for Recycling Waste Plastics To Fuel Gas Using a Moving-Bed Reactor.* Energy & Fuels, 2006. **20**: p. 155-158.

4. Ahmed, I.I. and A.K. Gupta, *Hydrogen production from polystyrene pyrolysis and gasification: Characteristics and kinetics.* International Journal of Hydrogen Energy, 2009. **34**(15): p. 6253-6264.

5. Czernik, S. and R.J. French, *Production of Hydrogen from Plastics by Pyrolysis and Catalytic Steam Reform.* Energy & Fuels, 2006. **20**: p. 754-758.

6. Namioka, T., et al., *Hydrogen-rich gas production from waste plastics by pyrolysis and low-temperature steam reforming over a ruthenium catalyst.* Applied Energy, 2011. **88**(6): p. 2019-2026.

7. Wu, C. and P.T. Williams, *Hydrogen production by steam gasification of polypropylene with various nickel catalysts.* Applied Catalysis B: Environmental, 2009. **87**(3-4): p. 152-161.

8. Wu, C. and P.T. Williams, *Investigation of Ni-Al, Ni-Mg-Al and Ni-Cu-Al catalyst for hydrogen production from pyrolysis–gasification of polypropylene.* Applied Catalysis B: Environmental, 2009. **90**(1-2): p. 147-156.

9. Wu, C. and P.T. Williams, *Pyrolysis–gasification of post-consumer municipal solid plastic waste for hydrogen production.* International Journal of Hydrogen Energy, 2010. **35**(3): p. 949-957.

10. Aupretre, F., C. Descorme, and D. Duprez, *Bio-ethanol catalytic steam reforming over supported metal catalysts.* Catalysis Communications, 2002. **3**: p. 263-267.

11. Sehested, J., *Four challenges for nickel steam-reforming catalysts.* Catalysis Today, 2006. **111**(1-2): p. 103-110.

12. Rostrup-Nielsen, J.R., *Steam Reforming Catalysts*. 1975, Copenhagen: Danish Technical Press.

13. Sato, K. and K. Fujimoto, *Development of new nickel based catalyst for tar reforming with superior resistance to sulfur poisoning and coking in biomass gasification.* Catalysis Communications, 2007. **8**(11): p. 1697-1701.

14. Srinakruang, J., et al., *A highly efficient catalyst for tar gasification with steam.* Catalysis Communications, 2005. **6**(6): p. 437-440.

15. Trimm, D.L., *Catalysts for the control of coking during steam reforming.* Catalysis Today, 1999. **49**: p. 3-10.

16. Wu, C. and P.T. Williams, *Investigation of coke formation on Ni-Mg-Al catalyst for hydrogen production from the catalytic steam pyrolysis-gasification of polypropylene.* Applied Catalysis B: Environmental, 2010. **96**(1-2): p. 198-207.

17. Kukovitskii, E.F., et al., *Carbon nanotubes of polyethylene.* Chemical Physics Letters, 1997. **266**: p. 323-328.

18. Nessim, G.D., *Properties, synthesis, and growth mechanisms of carbon nanotubes with special focus on thermal chemical vapor deposition.* Nanoscale, 2010. **2**(8): p. 1306-23.

19. Volder, M.F.L.D., et al., *Carbon Nanotubes: Present and Future Commercial Applications.* Science, 2013. **339**(6119): p. 535-539.

20. Acomb, J.C., C. Wu, and P.T. Williams, *Control of steam input to the pyrolysis-gasification of waste plastics for improved production of hydrogen or carbon nanotubes.* Applied Catalysis B: Environmental, 2014. **147**: p. 571-584.

21. Arena, U. and M.L. Mastellone, *Production of Multi-wall Carbon Nanotubes by Means of Fluidized Bed Pyrolysis of Virgin or Recycled Polymers.* Proceedings of ENS-European Nano System, Paris 2005, TIMA Editions, 2005: p. 7-12.

22. Arena, U., et al., *An innovative process for mass production of multi-wall carbon nanotubes by means of low-cost pyrolysis of polyolefins.* Polymer Degradation and Stability, 2006. **91**(4): p. 763-768.

23. Chung, Y.-H. and S. Jou, *Carbon nanotubes from catalytic pyrolysis of polypropylene.* Materials Chemistry and Physics, 2005. **92**(1): p. 256-259.

24. Kukovitsky, E.F., et al., *CVD growth of carbon nanotube films on nickel substrates.* Applied Surface Science, 2003. **215**(1-4): p. 201-208.

25. Kukovitsky, E.F., et al., *Correlation between metal catalyst particle size and carbon nanotube growth.* Chemical Physics Letters, 2002. **355**(5-6): p. 497-503.

26. Liu, J., et al., *Catalytic pyrolysis of polypropylene to synthesize carbon nanotubes and hydrogen through a two-stage process.* Polymer Degradation and Stability, 2011. **96**(10): p. 1711-1719.

27. Zhang, J.H., et al., *Synthesis and characterization of larger diameter carbon nanotubes from catalytic pyrolysis of polypropylene.* Materials Letters, 2008. **62**(12-13): p. 1839-1842.

28. Wu, C., et al., *Sustainable processing of waste plastics to produce high yield hydrogen rich synthesis gas and high quality carbon nanotubes.* RSC Advances, 2012. **2**: p. 4045-4047.

29. Ago, H., et al., *Gas analysis of the CVD process for high yield growth of carbon nanotubes over metal-supported catalysts.* Carbon, 2006. **44**(14): p. 2912-2918.

30. Amama, P.B., et al., *Role of Water in Super Growth of Single-Walled Carbon Nanotube Carpets.* Nano Letters, 2009. **9**(1): p. 44-49.

31. Govindaraj, A., et al., *An investigation of carbon nanotubes obtained from the decomposition of methane over reduced Mg1–xMxAl2O4 spinel catalysts.* Journal of Materials Research, 1999. **14**(6): p. 2567-2576.

32. Hata, K., et al., *Water-assisted highly efficient synthesis of impurity-free single-walled carbon nanotubes.* Science, 2004. **306**(5700): p. 1362-4.

33. Kong, J., A.M. Cassell, and H. Dai, *Chemical vapor deposition of methane for single-walled carbon nanotubes.* Chemical Physics Letters, 1998. **292**: p. 567-574.

34. Takenaka, S., *Formation of filamentous carbons over supported Fe catalysts through methane decomposition.* Journal of Catalysis, 2004. **222**(2): p. 520-531.

35. Tan, S.-M., et al., *Effects of FeOx, CoOx, and NiO catalysts and calcination temperatures on the synthesis of single-walled carbon nanotubes through chemical vapor deposition of methane.* Journal of Alloys and Compounds, 2009. **477**(1-2): p. 785-788.

36. Chai, S.-P., S.H. Sharif Zein, and A.R. Mohamed, *The effect of catalyst calcination temperature on the diameter of carbon nanotubes synthesized by the decomposition of methane.* Carbon, 2007. **45**(7): p. 1535-1541.

37. Lee, C.J., J.H. Park, and J. Park, *Synthesis of bamboo-shaped multiwalled carbon nanotubes using thermal chemical vapor deposition.* Chemical Physics Letters, 2000. **323**(5-6): p. 560-565.

38. Yeoh, W.-M., et al., *Synthesis of high purity multi-walled carbon nanotubes over Co-Mo/MgO catalyst by the catalytic chemical vapor deposition of methane.* New Carbon Materials, 2009. **24**(2): p. 119-123.

39. Lin, Y.-C. and J.-H. Lin, *Purity-controllable growth of bamboo-like multi-walled carbon nanotubes over copper-based catalysts.* Catalysis Communications, 2013. **34**: p. 41-44.

40. Liu, W.-W., et al., *Synthesis of Single-Walled Carbon Nanotubes: Effects of Active Metals, Catalyst Supports, and Metal Loading Percentage.* Journal of Nanomaterials, 2013. **2013**: p. 1-8.

41. Hu, X. and G. Lu, *Comparative study of alumina-supported transition metal catalysts for hydrogen generation by steam reforming of acetic acid.* Applied Catalysis B: Environmental, 2010. **99**(1-2): p. 289-297.

42. Nahil, M.A., C. Wu, and P.T. Williams, *Influence of metal addition to Ni-based catalysts for the co-production of carbon nanotubes and hydrogen from the thermal processing of waste polypropylene.* Fuel Processing Technology, 2014.

43. Ermakova, M.A. and D.Y. Ermakov, *Ni/SiO2 and Fe/SiO2 catalysts for production of hydrogen and filamentous carbon via methane decomposition.* Catalysis Today, 2002. **77**: p. 225-235.

44. Ermakova, M.A., et al., *New Nickel Catalysts for the Formation of Filamentous Carbon in the Reaction of Methane Decomposition.* Journal of Catalysis, 1999. **187**: p. 77-84.

45. Jourdain, V. and C. Bichara, *Current understanding of the growth of carbon nanotubes in catalytic chemical vapour deposition.* Carbon, 2013. **58**: p. 2-39.

46. Clause, O., et al., *Preparation and thermal reactivity of nickel/chromium and nickel/aluminium hydrotalcite-type precursors.* Applied Catalysis 1991. **73**: p. 217-236.

47. Furusawa, T., et al., *Hydrogen production from the gasification of lignin with nickel catalysts in supercritical water.* International Journal of Hydrogen Energy, 2007. **32**: p. 699-704.

48. Garcia, L., et al., *Influence of Calcination and Reduction Conditions on the Catalyst Performance in the Pyrolysis Process of Biomass.* Energy & Fuels, 1998. **12**: p. 139-143.

49. Chen, Y.-g. and J. Ren, *Conversion of methane and carbon dioxide into synthesis gas over alumina-supported nickel catalysts. Effect of Ni-A1$_2$0$_3$ interactions.* Catalysis Letters, 1994. **29**: p. 39-48.

50. Zieliński, J., *Morphology of nickel/alumina catalysts.* Journal of Catalysis, 1982. **76**(1): p. 157-163.

51. Heracleous, E., et al., *Investigation of Ni-based alumina-supported catalysts for the oxidative dehydrogenation of ethane to ethylene: structural characterization and reactivity studies.* Journal of Catalysis, 2005. **231**(1): p. 159-171.

52. Li, G., L. Hu, and J.M. Hill, *Comparison of reducibility and stability of alumina-supported Ni catalysts prepared by impregnation and co-precipitation.* Applied Catalysis A: General, 2006. **301**(1): p. 16-24.

53. Bolt, P.H., F.H.P.M. Habraken, and J.W. Geus, *Formation of Nickel, Cobalt, Copper, and Iron Aluminates from $\alpha\lambda\pi\eta\alpha$ $\alpha\nu\delta$ $\gamma\alpha\mu\mu\alpha$ Alumina Supported Oxides: A Comparative Study.* Journal of Solid State Chemistry, 1998. **135**: p. 59-69.

54. Gao, X., et al., *Reduction of Supported Iron Oxide studied by Temperature-programmed Reduction combined with Mossbauer Spectroscopy and X-Ray Diffraction* Journal of the Chemical Society, Faraday Transactions, 1993. **89**(7): p. 1079-1084.

55. Griboval-Constant, A., et al., *Cobalt and iron species in alumina supported bimetallic catalysts for Fischer–Tropsch reaction.* Applied Catalysis A: General, 2014. **481**: p. 116-126.

56. Park, J.-Y., et al., *Alumina-supported iron oxide nanoparticles as Fischer–Tropsch catalysts: Effect of particle size of iron oxide.* Journal of Molecular Catalysis A: Chemical, 2010. **323**(1-2): p. 84-90.

57. Ren-Yuan, T., et al., *An in situ combined temperature-programmed reduction-Mössbauer spectroscopy of alumina-supported iron catalysts.* Journal of Catalysis, 1987. **106**(2): p. 440-448.

58. Schanke, D., et al., *Study of Pt-Promoted Cobalt CO Hydrogenation Catalysts.* Journal of Catalysis, 1995. **156**: p. 85-95.

59. Luo, M.-F., et al., *In situ XRD, Raman, and TPR studies of CuO/Al2O3 catalysts for CO oxidation.* Journal of Molecular Catalysis A: Chemical, 2005. **239**(1-2): p. 243-248.

60. Marino, F.J., et al., *Hydrogen from steam reforming of ethanol. Characterization and performance of copper-nickel supported catalysts.* International Journal of Hydrogen Energy, 1998. **23**(12): p. 1095-1101.

61. Cheung, C.L., et al., *Diameter-Controlled Synthesis of Carbon Nanotubes.* Journal of Physical Chemistry B, 2002. **106**: p. 2429-2433.

62. Nasibulin, A., et al., *Correlation between catalyst particle and single-walled carbon nanotube diameters.* Carbon, 2005. **43**(11): p. 2251-2257.

63. Wang, P., et al., *Filamentous carbon prepared by the catalytic pyrolysis of CH4 on Ni/SiO2.* Applied Catalysis A: General, 2002. **231**: p. 34-44.

64. Jiang, Z.W., et al., *Polypropylene as a carbon source for the synthesis of multi-walled carbon nanotubes via catalytic combustion.* Carbon, 2007. **45**(2): p. 449-458.

65. Das, N., et al., *The effect of feedstock and process conditions on the synthesis of high purity CNTs from aromatic hydrocarbons.* Carbon, 2006. **44**(11): p. 2236-2245.

66. Tessonnier, J.-P. and D.S. Su, *Recent Progress on the Growth Mechanism of Carbon Nanotubes: A Review.* ChemSusChem, 2011. **4**(7): p. 824-847.

67. Moisala, A., A.G. Nasibulin, and E.I. Kauppinen, *The role of metal nanoparticles in the catalytic production of single-walled carbon nanotubes—a review.* Journal of Physics: Condensed matter, 2003. **15**: p. S3011-S3035.

68. Sengupta, J., et al., *Effect of growth temperature on the CVD grown Fe filled multi-walled carbon nanotubes using a modified photoresist.* Materials Research Bulletin, 2010. **45**(9): p. 1189-1193.

69. Malek Abbaslou, R.M., J. Soltan, and A.K. Dalai, *The effects of carbon concentration in the precursor gas on the quality and quantity of carbon nanotubes synthesized by CVD method.* Applied Catalysis A: General, 2010. **372**(2): p. 147-152.

70. Gallego, G.S., et al., *Production of hydrogen and MWCNTs by methane decomposition over catalysts originated from LaNiO(3) perovskite.* Catalysis Today, 2010. **149**(3-4): p. 365-371.

71. Allaouia, A., et al., *Mechanical and electrical properties of a MWNT/epoxy composite.* Composites Science and Technology, 2002. **62**: p. 1993-1998.

72. Montazeri, A., et al., *Mechanical properties of multi-walled carbon nanotube/epoxy composites.* Materials & Design, 2010. **31**(9): p. 4202-4208.

73. Rahaman, M.S., C.D. Vecitis, and M. Elimelech, *Electrochemical carbon-nanotube filter performance toward virus removal and inactivation in the presence of natural organic matter.* Environ Sci Technol, 2012. **46**(3): p. 1556-64.

74. Gao, G. and C.D. Vecitis, *Electrochemical carbon nanotube filter oxidative performance as a function of surface chemistry.* Environ Sci Technol, 2011. **45**(22): p. 9726-34.

75. Sotowa, C., et al., *The reinforcing effect of combined carbon nanotubes and acetylene blacks on the positive electrode of lithium-ion batteries.* ChemSusChem, 2008. **1**(11): p. 911-5.

76. Beigbeder, A., et al., *Preparation and characterisation of silicone-based coatings filled with carbon nanotubes and natural sepiolite and their application as marine fouling-release coatings.* Biofouling, 2008. **24**(4): p. 291-302.

77. Coleman, J.N., et al., *High-Performace Nanotube-Reinforced Plastics: Understanding the Mechanism of Strength Increase.* Advanced Functional Materials, 2004. **14**(8): p. 791-798.

Acknowledgement

The support from the UK Engineering and Physical Sciences Research Council for a

scholarship for one of us (JCA) is gratefully acknowledged

Table 1 Effect of catalyst metal on mass balance, gas composition and hydrogen conversion

Catalyst	Ni Al_2O_3	Fe Al_2O_3	Co Al_2O_3	Cu Al_2O_3
Metal (wt%)	10%	10%	10%	10%
Gas (wt%)	61.2	55.7	60.2	60.4
Oils (wt%)	26.6	18.4	29.8	31.9
Solid (wt%)	12.2	26.0	9.9	7.7
H_2 (vol%)	36.6	50.6	31.3	26.0
CH_4 (vol%)	23.6	19.8	24.9	26.6
C_2-C_4 (vol %)	39.8	29.6	43.8	47.4
Hydrogen conversion (% H in sample converted into gas)	16.5	26.8	12.8	10.1

Table 2: Effect of calcination temperature of nickel catalysts on mass balance, gas composition and hydrogen conversion

Calcination temperature (°C)	500	750
Gas (wt%)	60.8	61.2
Oils (wt%)	26.5	26.6
Solid (wt%)	12.7	12.2
H_2 (vol%)	34.1	36.6
CH_4 (vol%)	23.5	23.6
C_2-C_4 (vol %)	42.4	39.8
Hydrogen conversion (% H in sample converted into gas)	15.2	16.5

Figure captions

1. Schematic diagram of the experimental setup
2. TEM images of fresh catalysts. Ni/Al_2O_3, (b) Fe/Al_2O_3, (c) Co/Al_2O_3 and (d) Cu/Al_2O_3
3. XRD investigation of the fresh catalysts
4. Investigation of the fresh catalysts by Temperature programmed reduction
5. Scanning electron microscopy of the carbon deposits on the used catalysts: (a) Ni/Al_2O_3, (b) Fe/Al_2O_3, (c) Co/Al_2O_3 and (d) Cu/Al_2O_3
6. Transmission electron microscopy of the carbon deposits on the used catalysts: (a) Ni/Al_2O_3, (b) Fe/Al_2O_3, (c) Co/Al_2O_3 and (d) Cu/Al_2O_3
7. XRD investigation of the used catalysts
8. Temperature programmed oxidation investigation of the used catalysts: (a) Derivative TPO plot and (b) Amount of different carbon types deposited on the catalysts
9. Investigation of the used catalysts by Raman spectroscopy: Ni/Al_2O_3, (b) Fe/Al_2O_3, (c) Co/Al_2O_3 and (d) Cu/Al_2O_3
10. Analysis of the fresh Nickel500 catalyst: (a) TEM image, (b) XRD and (c) TPR
11. Analysis of the used Nickel500 catalyst (a) SEM, (b) Raman spectroscopy and (c) TEM
12. The effect of calcination temperature on the yield of CNTs: (a) Derivative TPO graph and (b) Amount of different carbon types deposited on the catalysts

Figure 1: Schematic diagram of the experimental setup

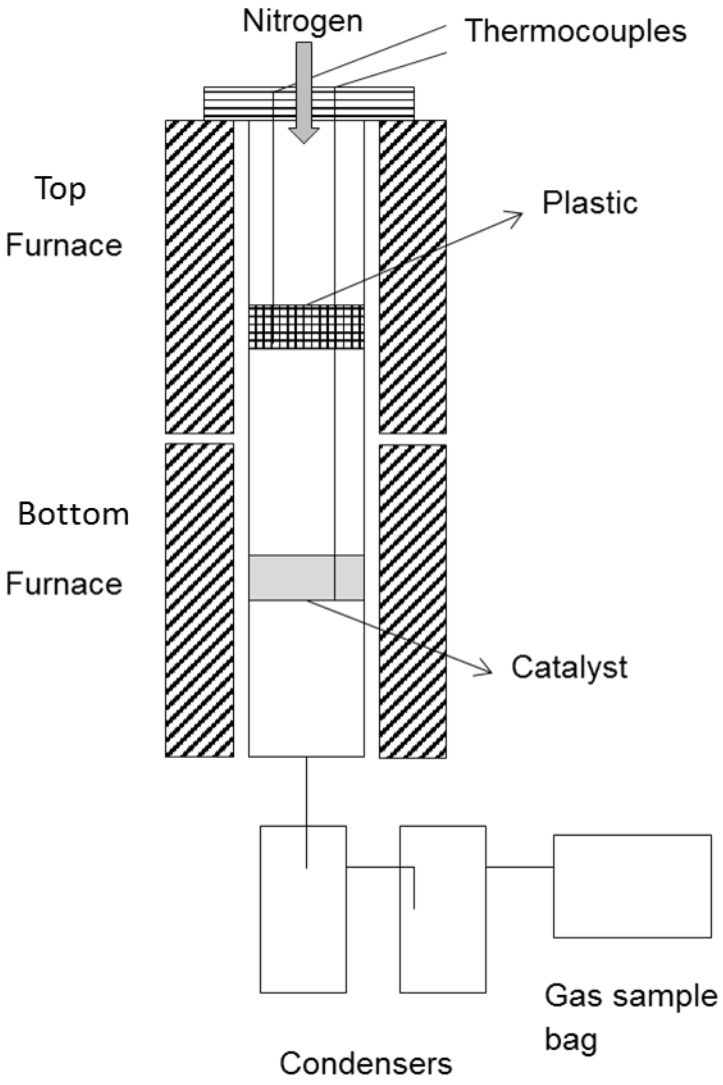

Figure 2: TEM images of fresh catalysts. Ni/Al_2O_3, (b) Fe/Al_2O_3, (c) Co/Al_2O_3 and (d) Cu/Al_2O_3

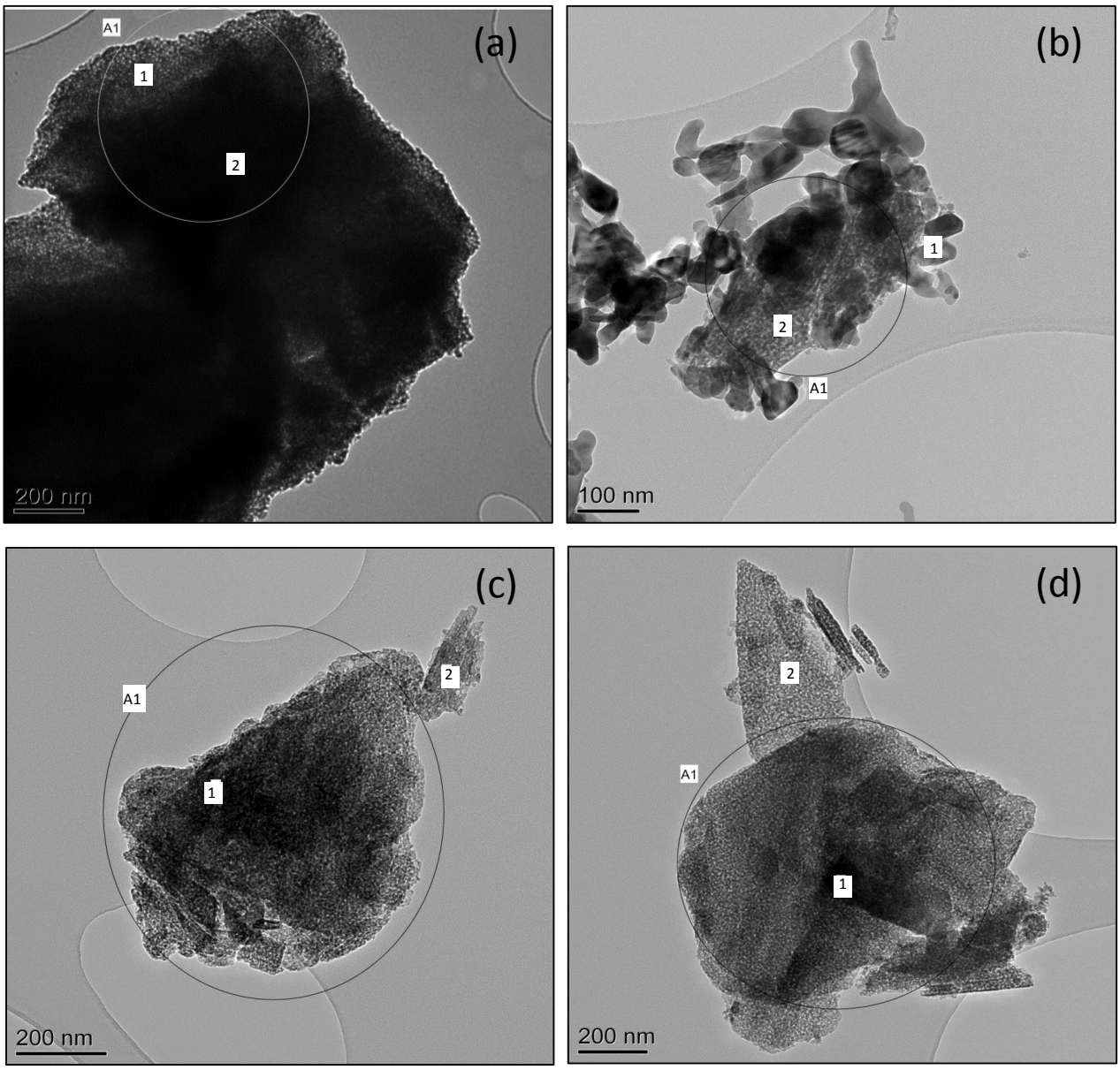

Figure 3: XRD investigation of the fresh catalysts

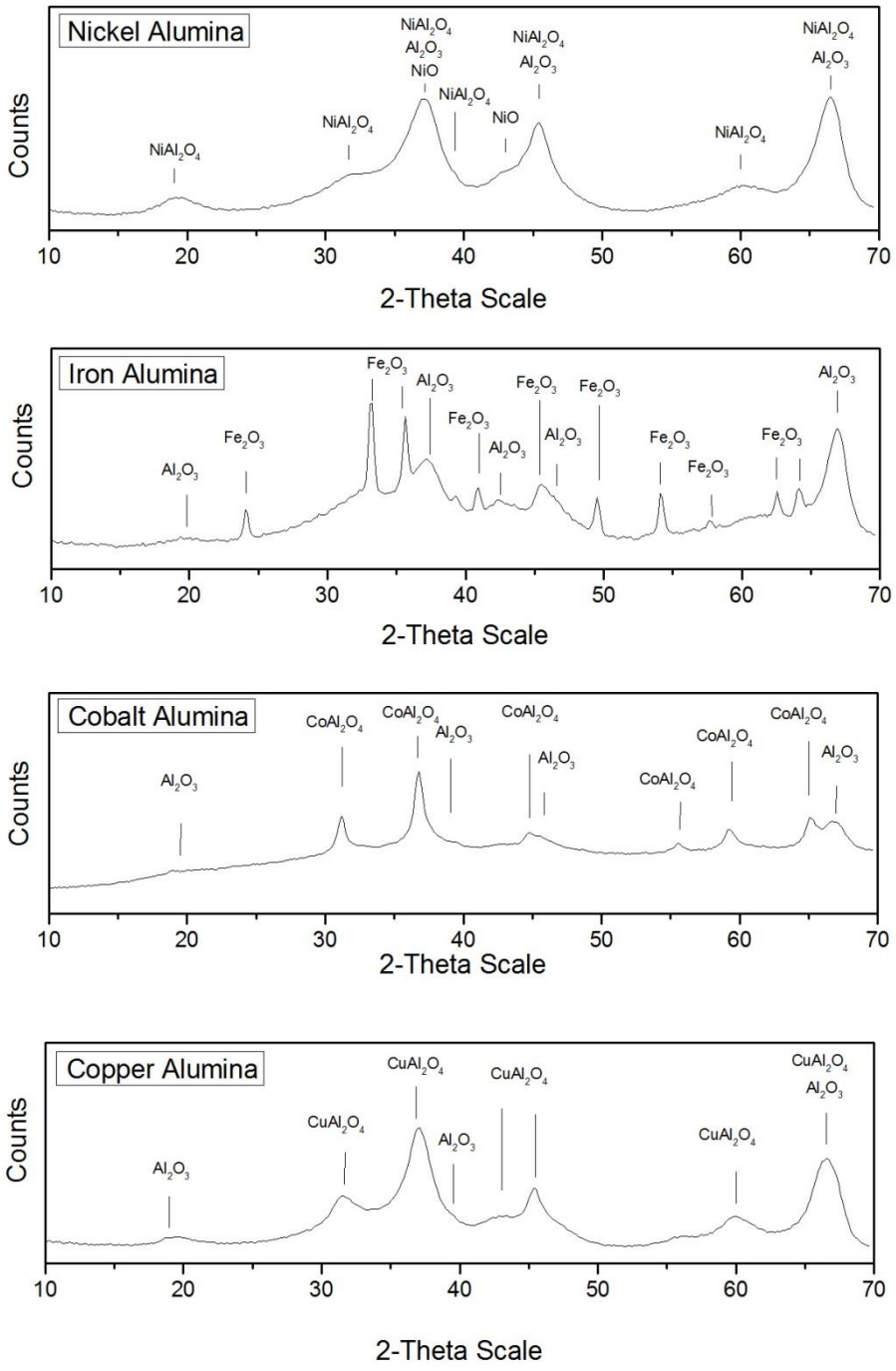

Figure 4: Investigation of the fresh catalysts by temperature programmed reduction

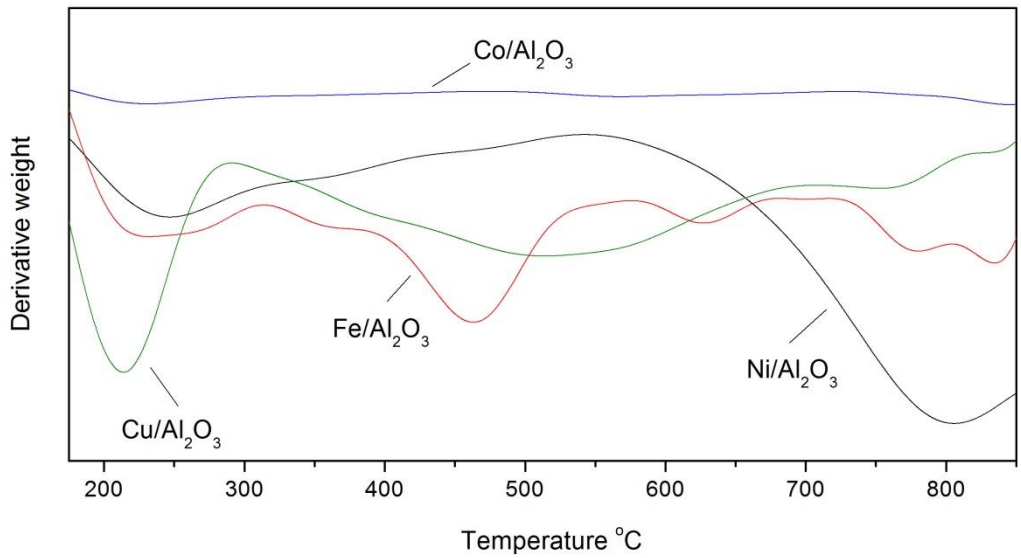

Figure 5: Scanning electron microscopy of the carbon deposits on the used catalysts: (a) Ni/Al_2O_3, (b) Fe/Al_2O_3, (c) Co/Al_2O_3 and (d) Cu/Al_2O_3

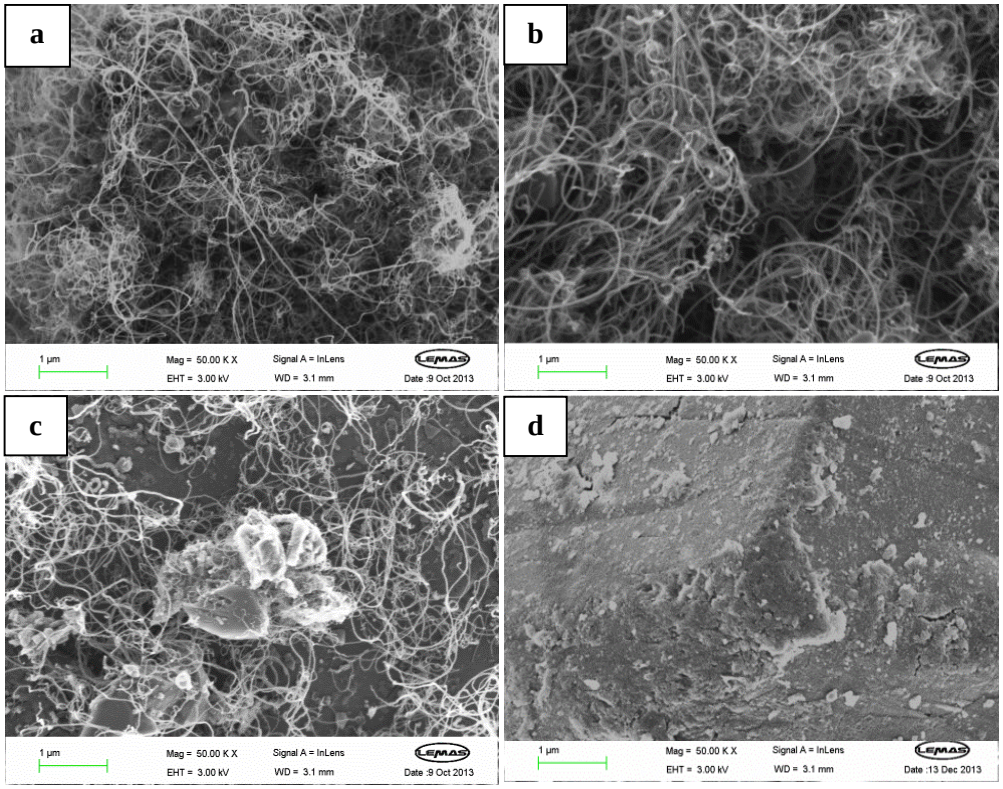

Figure 6: Transmission electron microscopy of the carbon deposits on the used catalysts: (a) Ni/Al_2O_3, (b) Fe/Al_2O_3, (c) Co/Al_2O_3 and (d) Cu/Al_2O_3

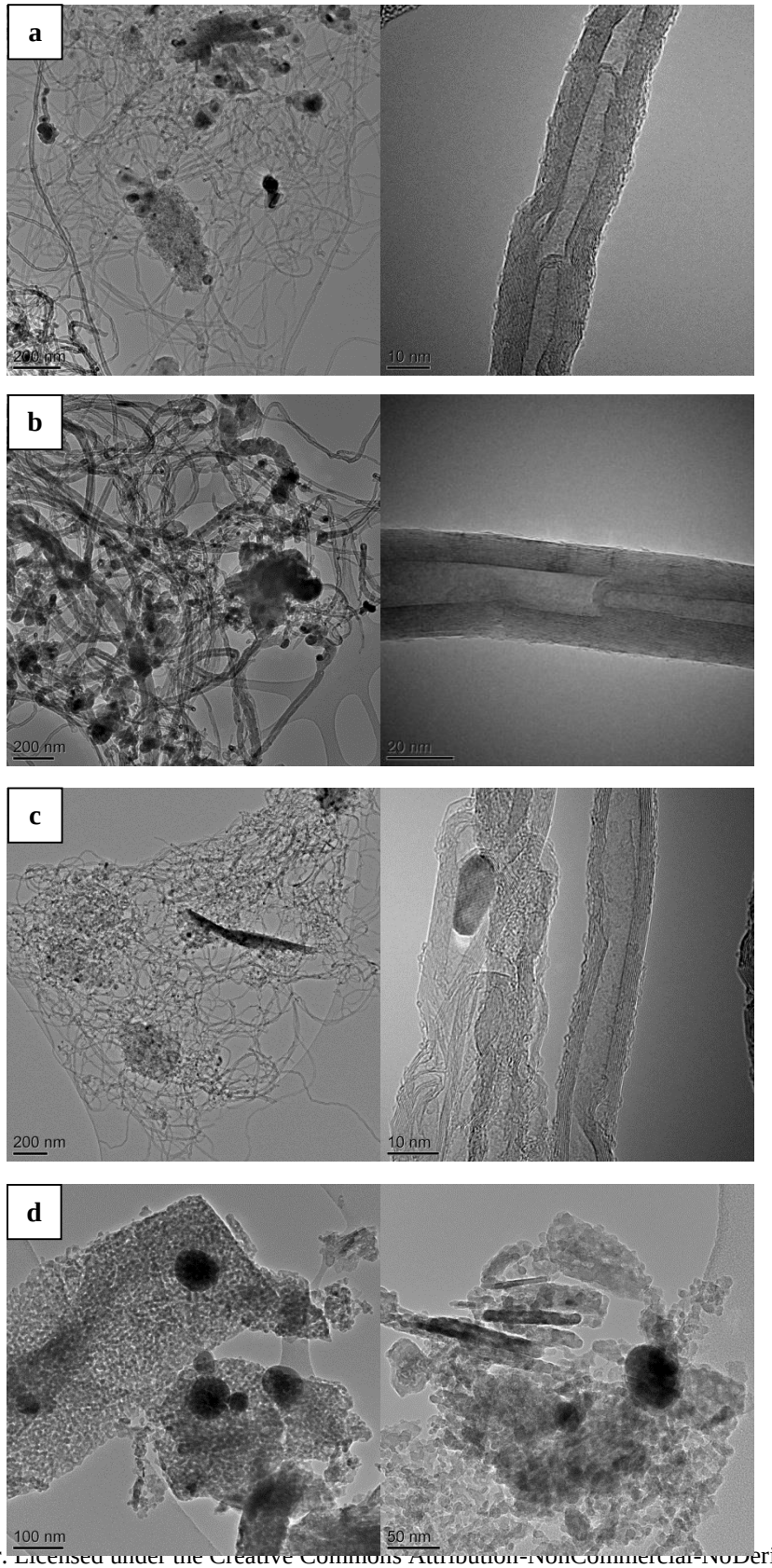

Figure 7: XRD investigation of the used catalysts

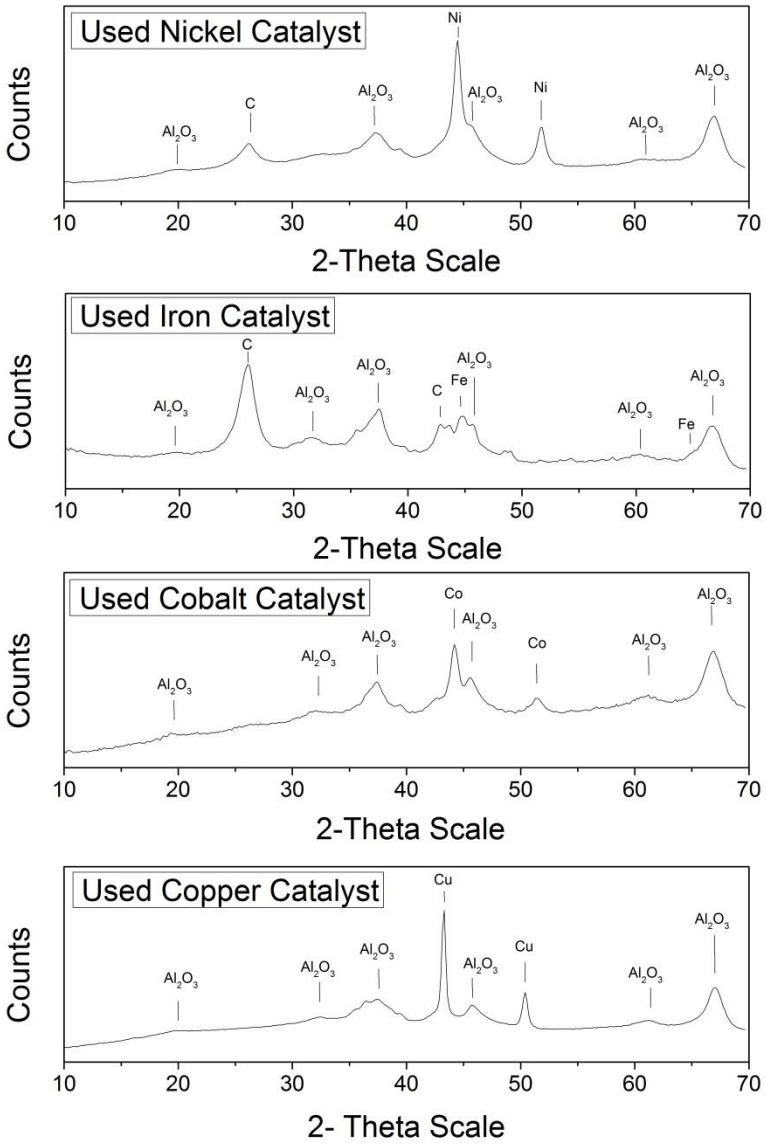

Figure 8: Temperature programmed oxidation investigation of the used catalysts: (a) Derivative TPO plot and (b) Amount of different carbon types deposited on the catalysts

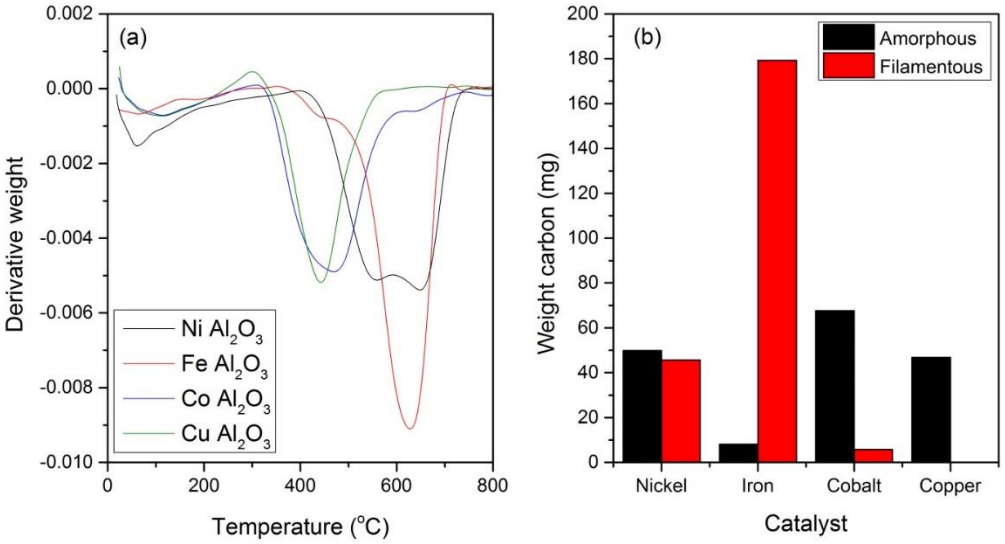

Figure 9: Investigation of the used catalysts by Raman spectroscopy: Ni/Al_2O_3, (b) Fe/Al_2O_3, (c) Co/Al_2O_3 and (d) Cu/Al_2O_3

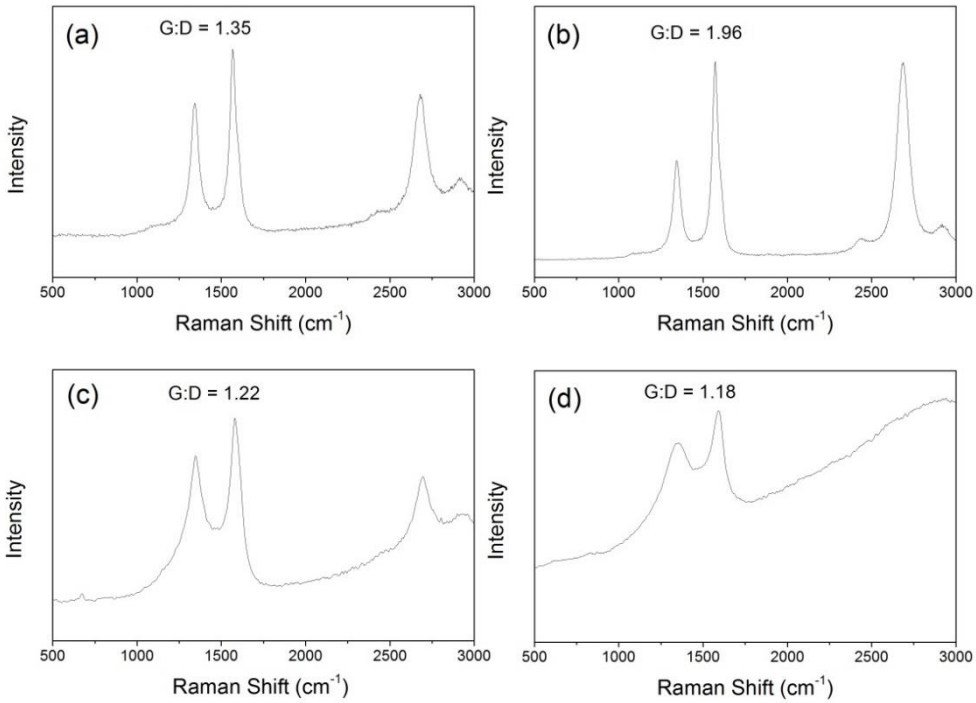

Figure 10: Analysis of the fresh Nickel500 catalyst: (a) TEM image, (b) XRD and (c) TPR

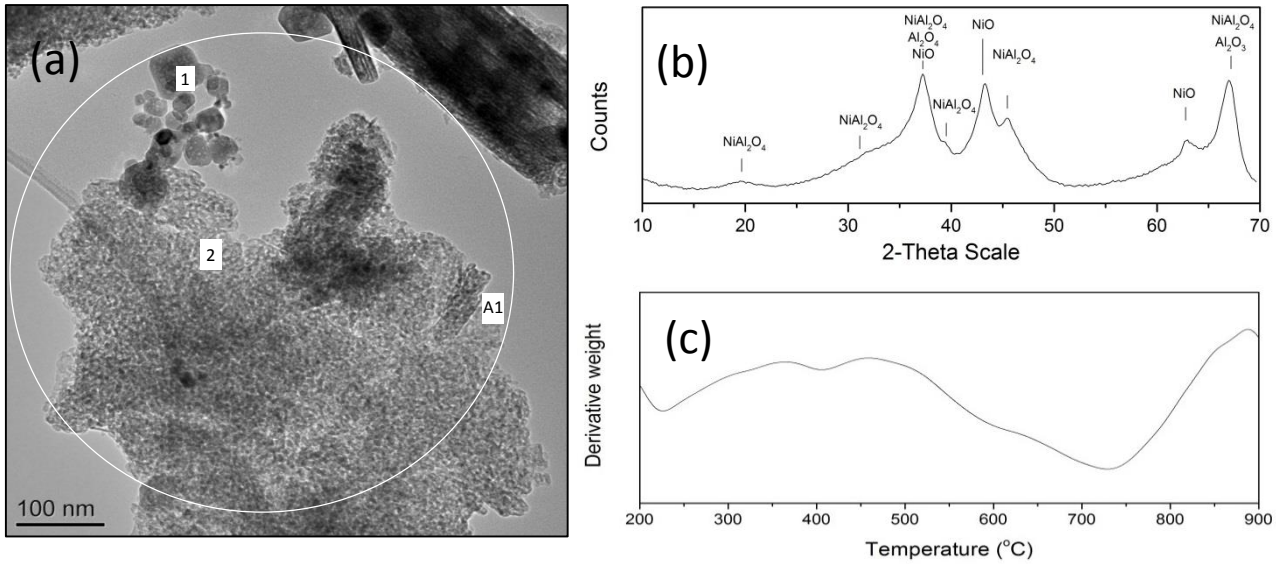

Figure 11: Analysis of the used Nickel500 catalyst (a) SEM, (b) Raman spectroscopy and (c) TEM

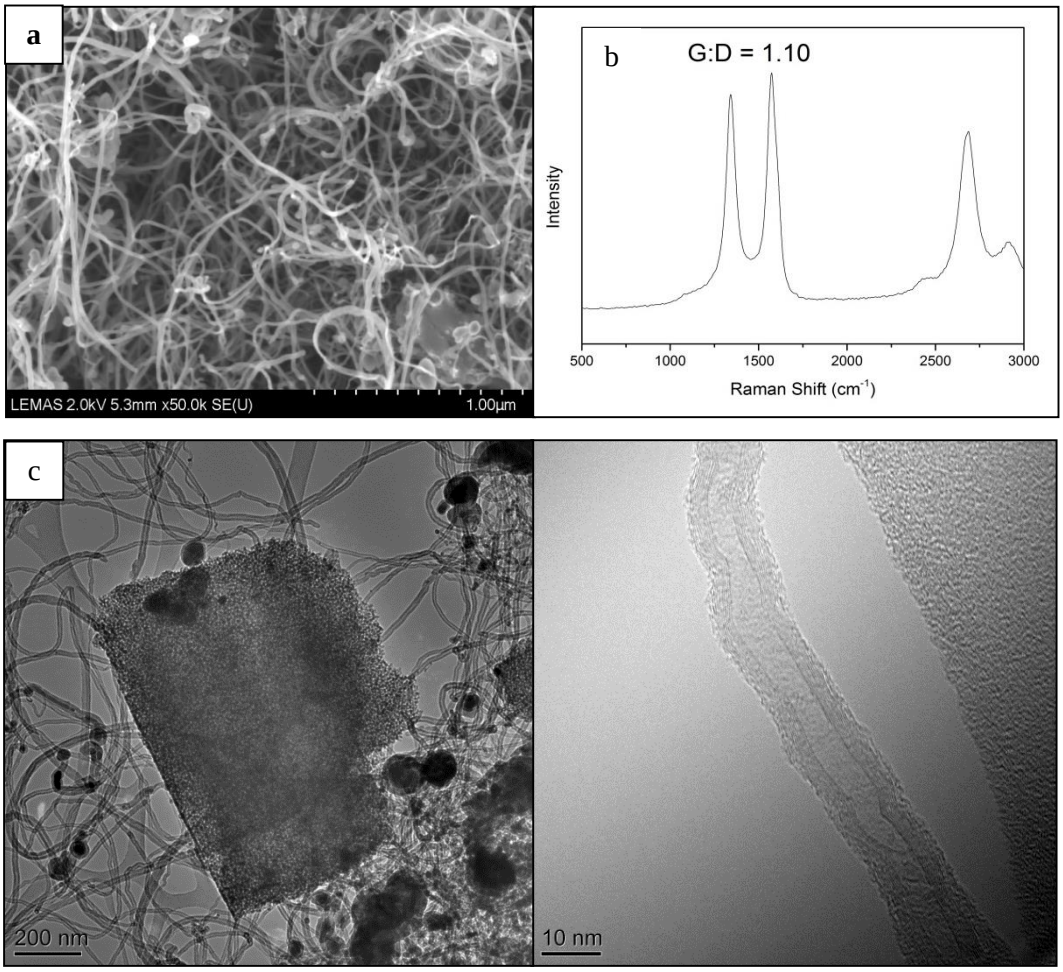

Figure 12: The effect of calcination temperature on the yield of CNTs: (a) Derivative TPO graph and (b) Amount of different carbon types deposited on the catalysts

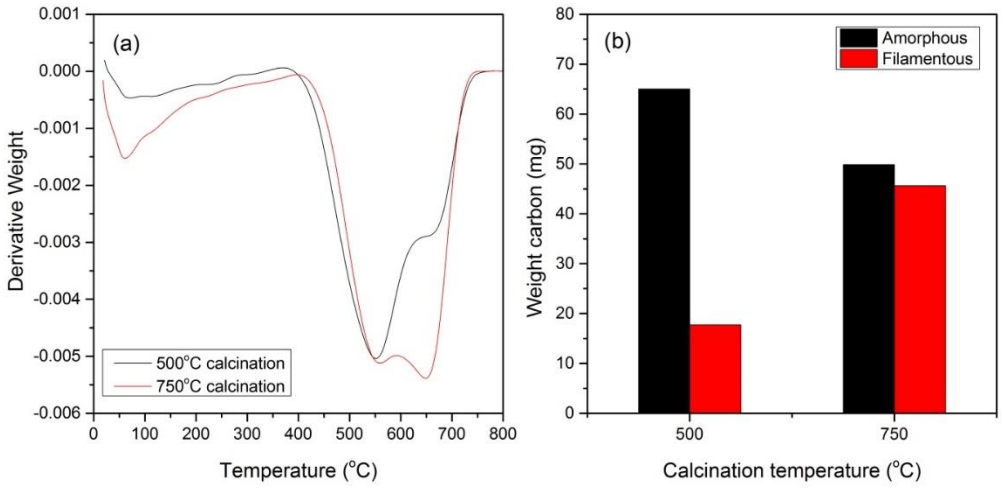

Supporting information

1. EDX spectrums of TEM image of nickel catalyst shown in Figure 2(a): (a) Area A1, (b) Point 1, (c) Point 2

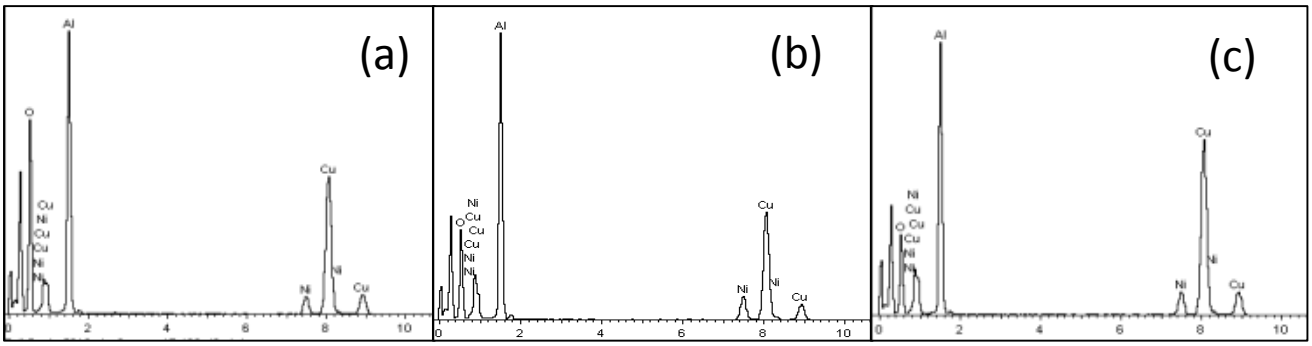

2. EDX spectrums of TEM image of iron catalyst shown in shown in Figure 2(b): (a) Area A1, (b) Point 1, (c) Point 2

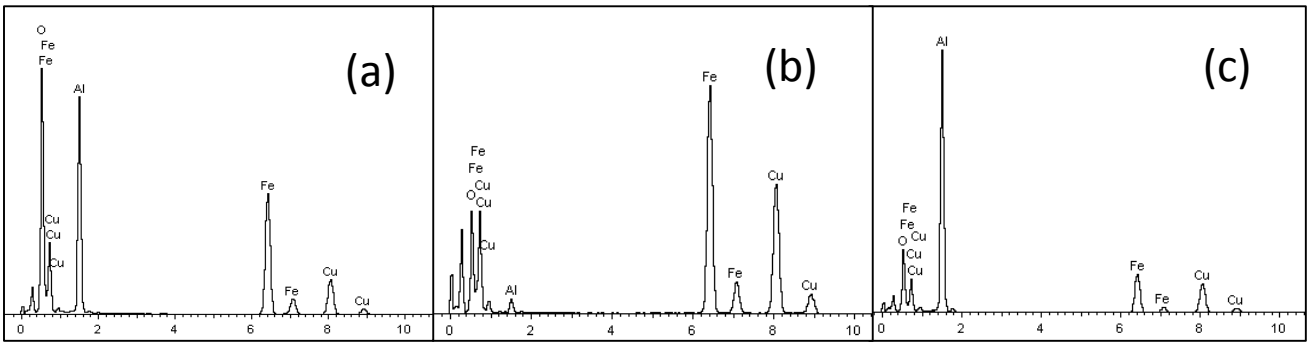

3. EDX spectrums of TEM image of cobalt catalyst shown in shown in Figure 2(c): (a) Area A1, (b) Point 1, (c) Point 2

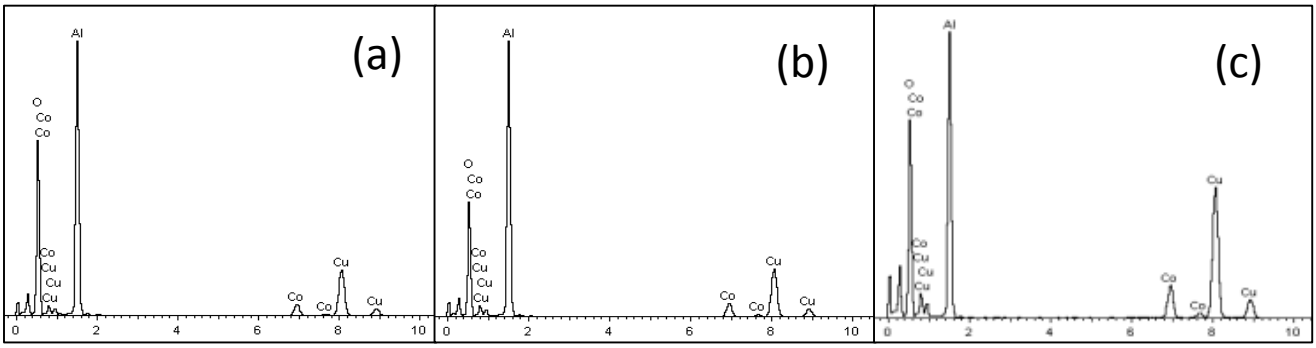

4. EDX spectrums of TEM image of copper catalyst shown in shown in Figure 2(d): (a) Area A1, (b) Point 1, (c) Point 2

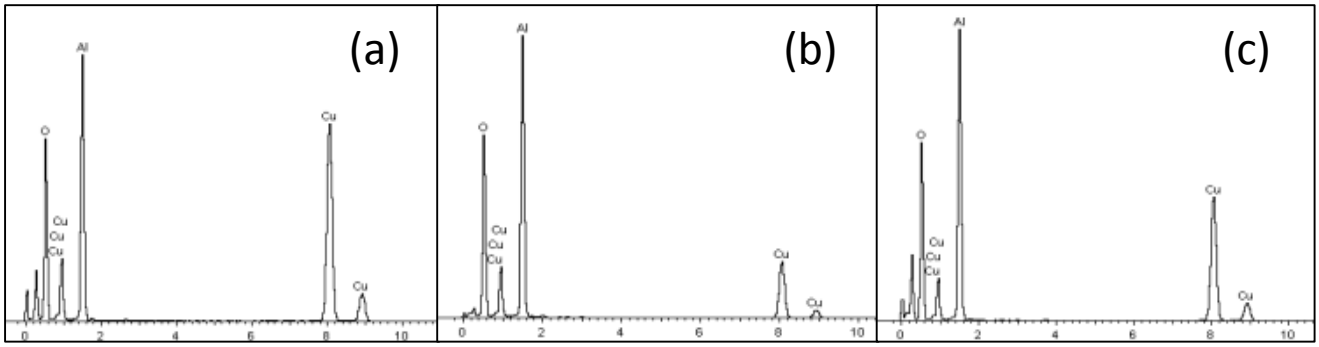

5. EDX spectrums of TEM image of nickel500 catalyst shown in shown in Figure 10(a): (a) Area A1 , (b) Point 1, (c) Point 2